AMERICAN UNIVERSITY OF BEIRUT

EULERIAN-LAGRANGIAN MODEL FOR DOWNSCALING WIND FIELDS AND PARTICLES DISPERSION WITH APPLICATION TO BEIRUT CITY

by
ALI MOHAMMAD SALEH

A thesis proposal
submitted in partial fulfillment of the requirements
for the degree of Doctor of Philosophy
to the Department of Mechanical Engineering
of the Maroun Semaan Faculty of Engineering and Architecture
at the American University of Beirut

Beirut, Lebanon
September, 2020

AMERICAN UNIVERSITY OF BEIRUT

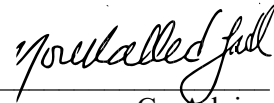## Eulerian-Lagrangian Model for Downscaling Wind Fields and Particles Dispersion with Application to Beirut
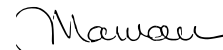by
ALI SALEH

Approved by:

_____

Dr. Issam Lakkis, Chairperson & Professor   Advisor
Department of Mechanical Engineering

_____

Dr. Fadl Moukalled, Professor   Co-Advisor
Department of Mechanical Engineering

_____

Dr. Marwan Darwish, Professor   Member of Committee
Department of Mechanical Engineering

Date of thesis defense: September 7, 2020

AMERICAN UNIVERSITY OF BEIRUT

THESIS RELEASE FORM

Student Name: _____ Saleh Ali Mohamad _____

Last   First   Middle

I authorize the American University of Beirut, to: (a) reproduce hard or electronic copies of my thesis; (b) include such copies in the archives and digital repositories of the University; and (c) make freely available such copies to third parties for research or educational purposes:

☑ As of the date of submission

☐ One year from the date of submission of my thesis.

☐ Two years from the date of submission of my thesis.

☐ Three years from the date of submission of my thesis.

Ali Saleh _____ September 14, 2020

Signature   Date

(This form is signed & dated when submitting the thesis to the University Libraries ScholarWorks)

ABSTRACT
OF THE THESIS OF

Ali Mohammad Saleh   for   Master of Engineering
     Major: Mechanical Engineering

Title: Eulerian-Lagrangian Model for Downscaling Wind Fields and Particles Dispersion with Application to Beirut City

The study of pollutant dispersion in urban areas is complex due to its dependency on the atmospheric boundary layer (ABL) flow and the near buildings perturbed flow. Computational fluid dynamics (CFD) models with the RANS turbulent closure schemes are a good compromise between accuracy and computational cost when solving such problems. In this study, we created a tool for solving wind flow in urban areas using the prognostic approach that is based on CDF models, and the diagnostic approach that is based on imposing mass continuity by solving an optimization equation. However, the use of standard RANS closure schemes with standard sand-grain rough wall function in the prognostic model show inconsistency with inlet conditions. To solve this issue, we implemented a new formulation of the Richards and Hoxey wall function and a modification of the k-ε model, and we derived a modification for the k-ω model. We implemented two methods for calculating the concentration field. The first one is under the Eulerian framework by solving the concentration transport equation and the second one under the Lagrangian framework by using the particle method with core radius spreading for diffusion. We tested the flow and dispersion models by simulating the wind field in an empty domain using different variations with k-ε and k-ω models. Then, by simulating the flow and particles dispersion around a building using the modified k-ε and k-ω models with the new wall function formulation and using the k-ω SST by resolving the viscous sublayer. Moreover, we simulated the flow field using the modified k-ε model for a domain containing an array of buildings.

TABLE OF CONTENTS

ILLUSTRATIONS

Figure

TABLES

CHAPTER I

IMPLEMENTATION AND GOVERNING EQUATIONS

A. Introduction

The study of air pollution in dense urban areas has become a vital topic in the past decades because of the increasing concerns about the quality of life and sustainability. The quantification of urban wind flow and air pollution helps authorities in managing air quality and designing the built environment in a healthy and comfortable way. However, air pollution modeling is complicated by its dependency on atmospheric flow and flow around buildings. Laboratory experiments for studying pollution dispersion in urban areas are costly [1, 2], and difficult to apply in practical applications. With the rapid development in computational power and models, numerical models have become standard tools to simulate flow and pollutant dispersion configurations around various building patterns. Gaussian-type dispersion models often used for predicting air pollution around building like CALPUFF and AERMOD are good for concentration fields far from obstacles. However, they are difficult to apply for complex geometrical domains.

On the other hand, computational fluid dynamics (CFD) approaches that are based on predicting the wind field by solving the Navier-Stokes equations coupled with the problem descriptive equations have become a promising tool for particle dispersion calculations in urban environment. This approach, which is based on solving the Navier Stokes equations, is known as prognostic wind modeling for its ability to forecast the time evolution of the atmospheric system. A less accurate alternative is the diagnostic modeling that is based on imposing continuity of mass on an interpolated

meteorological wind field. Such approach is suitable for getting quick solution due to their low computational costs. In both prognostic and diagnostic models, the concentration field can be calculated by solving a concentration transport equation or by using a particle solution method.

Mass-consistent diagnostic models impose continuity by solving an optimization equation developed based on variational analysis [3-5]. Several mass-consistent models have been developed, and many of them have been applied to simulate wind fields and transport of particles. The differences among these models are related to the way the initial wind field is constructed, the method for calculating the equation weights, and the method of solving the equations. The divergence-free wind flow model MATHEW was developed by Sherman [6] to provide wind field for the ADPIC pollutant transport model [7], and applied for the geysers drainage flow region in California [8], for a region in Colorado [9], and for the Apennine Mountains during the Lago Brasimone experimental campaign [10]. NUATMOS mass-consistent model [11] was developed and used to simulate tracer transport of the Cinder Cone Butte experiment [12]. The mass consistent model NOABL [13] simulated wind flow over the Blashaval Hill [14, 15]. Also, it is tested with the COMPLEX wind model [16] in three regions of the UK, and they are modified to solve problems that appeared while testing, leading to the development of a new MC-3 wind model [17]. Mass-consistent wind models were used for downscaling purposes, as they were used for increasing the wind fields' resolution generated by Global Circulation Models, and for regional-scale dispersion meteorological pre-processing [18, 19]. Another application for diagnostic wind field models was an instantaneous simulation for pollution control networks in an industrial plant [20].

The above diagnostic models are not suitable to calculate wind flows over complex geometries, or for getting accurate results when the flow is turbulent. For that purpose, prognostic models are more appropriate. The prognostic approach for solving turbulent flows can be divided broadly into the following categories: the direct numerical simulation (DNS) approach, the large-eddy simulation (LES) approach, and the Reynolds-averaged Navier-stokes (RANS) approach. DNS requires very high computational costs, LES on the other hand, has high but acceptable computational cost for simple turbulent flow and dispersion problems [21, 22], while the RANS approach is currently the most feasible for industrial size applications [23, 24]. Several RANS turbulence closure models like the standard k-ε model [25], the k-ε realizable model [26], the k-ε renormalized grouped model (RNG) [27], the k-ω standard model (SKO) [28-30] and the k-ω shear stress model (SST) [31] were developed and used for wind and dispersion modeling in urban areas. Nonetheless there is a continuous effort to improve these models and to overcome their drawbacks. At the moment, none of these models is capable of accurately predicting solutions over the whole domain of study [32], and each of them is suitable for a particular class of problems [33]. Thus, the choice of turbulence model for complex urban environments is still not well explained theoretically [34].

For ABL flow problems, the approaching flow should be modeled as horizontally homogenous as it is not the intention to model the development of inlet conditions since they are fully developed. For this purpose, Richards and Hoxey [35] proposed boundary conditions that are consistent with the k-ε turbulence closure. Generally, an ABL domain can be divided into three parts, that are the upstream and downstream regions where buildings are modeled implicitly using rough wall functions,

and the central region where buildings are modeled explicitly using their real geometries. Usually roughness is treated using sand-grain roughness based wall function [36] that is a modification of standard wall functions [37]. However, Blocken et al. [38] explained that the law of the wall for rough surfaces when modeling buildings implicitly is not consistent with the inlet profiles proposed by Richards and Hoxey [35]. In addition, Richards and Hoxey [35] proposed a constant turbulent kinetic energy inlet profile, which contradicts experimental measurements. Consequently, [39] derived analytically variable inlet profile for turbulent kinetic energy that satisfy measurements, but without fully studying its effect on the used model. Accordingly, Parente et al. [40] modified the k-ε model to insure its consistency with the variable k profile, and they proposed new implementation of wall function based on aerodynamic roughness to overcome the limitations of the sand-grain rough wall functions documented by Blocken et al. [38].

In this study we developed a tool capable of simulating wind flow and particles dispersion using the prognostic and diagnostic approaches. In the prognostic model, we used the SIMPLE algorithm with several turbulent closure schemes. We have implemented and tested the measures proposed by Richards and Hoxey, Yang et al., Gu et al. and Parente et al. [35, 39, 40] to obtain equilibrium between the k-ε turbulence model, inlet profiles and wall function. Also, we modified the k-ω turbulence model in a similar manner, and compared it with the modified k-ε model. We implemented two ways for modeling emissions, the first one using the Eulerian framework by solving a concentration transport equation, and the second one using the Lagrangian framework by using a particle method with core radius spreading for diffusion calculation. Wind

flow models are validated using CEDVAL A1-1 and CEDVAL B1 wind tunnel experiments while dispersion models are validated using CEDVAL A1-5 experiment.

B. Mesh Generation

We formulated a FORTRAN code to generate meshes automatically for cities, and we used it to generate a mesh for Beirut city. To use the code, you should provide it with a point cloud of the city's terrain and buildings' data files. According to user input, the code generates the buildings and terrain STL geometry files. Then, it uses terrainBlockMesher OpenFOAM utility [41, 42] to create the background mesh based on the generated "Terrain STL file". After that, using the SnappyHexMesh OpenFOAM utility, it creates a semi-final mesh based on the back ground mesh and the buildings' geometry file. Finally, it refines the grid around buildings and terrain to meet the required first near-wall boundary cell length for turbulence models. The code simplifies the process of meshing by writing all the required OpenFOAM utilities in a file where the user can specify all the details of the mesh. Also, we provide the code with the option to run in parallel to accelerate the process.

For simple geometries and small domains, we generated meshes using blockMesh OpenFOAM utility by dividing the domain into a number of blocks. To ease this division, we wrote a MATLAB code that can write blockMeshDict based on simple user specifications.

C. Wind Flow Models

1. Diagnostic model

The diagnostic model is an approximate but very fast model that works by interpolating the observed wind data in the domain, then attempts to have a divergence

free flow field while minimizing the change from the interpolated initial field. To interpolate the measured data, first we started by interpolating in the vertical direction using the power law scheme (Eq. (1)), then in the horizontal directions using the nearest few measurements weighted inversely by the square root of the distance (Eq. (2)) as

$$u = u_o \left(\frac{Z}{Z_0}\right)^p \tag{1}$$

$$V_a = \frac{\sum_{i=1}^{n} \frac{V_i}{r_i^2}}{\sum_{i=1}^{n} \frac{1}{r_i^2}} \tag{2}$$

In Eq. (1) u_0 and u are the measured and the calculated velocities respectively, Z_0 and Z are the altitudes of the measured and the calculated velocities, and p is an exponent obtained from the atmospheric stability conditions [41].

Finding the final mass-conserving wind field, with the minimal change from initial field is done by solving an elliptic partial differential equation for a Lagrange multiplier λ (Eq. (3)) then updating the velocities according to the Euler–Lagrange equations (Eq. (4)) [3, 6].

$$\frac{\partial^2 \lambda}{\partial x_1^2} + \frac{\partial^2 \lambda}{\partial x_2^2} + \frac{\alpha_1^2}{\alpha_2^2} \frac{\partial^2 \lambda}{\partial x_3^2} = -2\alpha_1^2 \frac{\partial \hat{u}_i}{\partial x_i} \tag{3}$$

$$u_1 = \hat{u}_1 + \frac{1}{2\alpha_1^2} \frac{\partial \lambda}{\partial x_1}, \quad u_2 = \hat{u}_2 + \frac{1}{2\alpha_1^2} \frac{\partial \lambda}{\partial x_2}, \quad u_3 = \hat{u}_3 + \frac{1}{2\alpha_2^2} \frac{\partial \lambda}{\partial x_3} \tag{4}$$

There are two boundary conditions that used to solve the elliptic optimization equation with the diagnostic approach. These are the closed (Eq. (5)) and the flow

through boundary (Eq. (6)) conditions. The closed boundary condition is applied for

terrain and buildings while the open or flow through boundary condition is applied for

all other non-solid boundary patches.

$$\frac{\partial \lambda}{\partial n} = 0, \quad \frac{\partial \lambda}{\partial e} \neq 0, \quad u = 0 \tag{5}$$

$$\frac{\partial \lambda}{\partial e} = 0, \quad \frac{\partial \lambda}{\partial n} \neq 0, \quad \lambda = 0 \tag{6}$$

2. *Prognostic model*

In our code, we used the SIMPLE algorithm with several standard turbulence

closures to simulate the flow. To overcome the limitation and inaccuracy of standard

turbulence models and sand grain rough wall functions, we implemented modifications

to the standard k-ε model, derived similar modifications to the standard k-ω model, and

implemented new rough wall functions suitable for ABL simulations.

For homogenous, incompressible and stead flow, we can assume a constant pressure,

zero vertical velocity, and constant shear stress. Thus, the two-dimensional forms of the

momentum, turbulent kinetic energy, and turbulent dissipation rate equations become

$$\mu_t \frac{\partial u}{\partial z} = \tau_w = \rho u^{*2} \tag{7}$$

$$\frac{\partial}{\partial z}\left(\frac{\mu_t}{\sigma_k}\frac{\partial k}{\partial z}\right) + G_k - \rho\varepsilon = 0 \tag{8}$$

$$\frac{\partial}{\partial z}\left(\frac{\mu_t}{\sigma_\varepsilon}\frac{\partial \varepsilon}{\partial z}\right) + C_{\varepsilon 1}G_k\frac{\varepsilon}{k} - C_{\varepsilon 2}\rho\frac{\varepsilon^2}{k} = 0 \tag{9}$$

The production of turbulent kinetic energy is $G_k = \mu_t(\partial u / \partial z)^2$, and the

turbulent viscosity is $\mu_t = \rho C_\mu k^2 / \varepsilon$, where σk, σε, Cε1, Cε2 and Cµ are k-ε model

parameters. ABL inlet profiles are generally fully developed, so to insure the

consistency between them and turbulence models, Richards and Hoxey [35] developed

a set of boundary conditions satisfying Eq. (7)-(9). The inlet boundary conditions are

$$u^* = \frac{\kappa U_h}{\ln\left(\dfrac{h + z_0}{z_0}\right)} \tag{10}$$

$$u = \frac{u^*}{\kappa} \ln\left(\frac{z + z_0}{z_0}\right) \tag{11}$$

$$k = \frac{u^{*2}}{\sqrt{C_\mu}} \tag{12}$$

$$\varepsilon = \frac{u^{*3}}{\kappa(z + z_0)} \tag{13}$$

where z_0 is the surface roughness height, κ is the Von Karman constant, u^* is the

frictional velocity, and U_h is a known velocity at reference height h. Similarly, at walls

$$u_g^* = \frac{\kappa U_g}{\ln\left(\dfrac{z_g + z_0}{z_0}\right)} \tag{14}$$

$$\tau_g = \rho u_g^{*2} \tag{15}$$

14

$$k_g = \frac{u_g^{*2}}{\sqrt{C_\mu}} \tag{16}$$

$$\varepsilon_g = \frac{\sqrt{C_\mu}\, k\, u_g^*}{\kappa(z_g + z_0)} \tag{17}$$

where U_g, k_g and ε_g are velocity, turbulent kinetic energy and turbulent dissipation rate values at boundary cell centroid. For the top patch, a constant shear stress $\tau = \rho u^{*2}$ was recommended. The drawback of Richards and Hoxey [35] inlet profiles is that the constant k inlet profile (Eq. (12)) contradicts with experimental data. To overcome this limitation, Yang et al. [39] mentioned that the turbulent kinetic energy increases with height and derived analytically its profile as

$$k(z) = \sqrt{C_1 \ln(z + z_0) + C_2} \tag{18}$$

where C_1 and C_2 are determined by curve fitting the experimental data. Yang et al. [39] argued that the new profile satisfies the k equation for neutrally stratified flow, but they didn't study the effect of non-constant k profile on the momentum and ε equations. For that, Parente et al. [40] derived a modification to the k-ε model to enable using any non-constant k inlet profile. First, they proved that, for equilibrium between generation and dissipation of turbulence, Eq. (11)-(13) are the solution to Eq. (7)-(9) if the turbulent dissipation Prandtl number is given by

$$\sigma_\varepsilon = \frac{\kappa^2}{(C_{\varepsilon 2} - C_{\varepsilon 1})\sqrt{C_\mu}} \tag{19}$$

The dissipation rate profile and the turbulence model parameter can be written as

$$\varepsilon(z) = \sqrt{C_\mu} k \frac{du}{dz}, \qquad C_\mu(z) = \frac{u^{*4}}{k(z)^2} \tag{20}$$

Then, by substituting $C_\mu(z)$ and $k(z)$ in Eq. (8), the following additional source term appears:

$$S_k(z) = \frac{\rho u^* \kappa}{\sigma_k} \frac{\partial}{\partial z}\left((z + z_0) \frac{\partial k}{\partial z} \right) \tag{21}$$

This source term should be added to the turbulent kinetic energy equation to insure equilibrium between non-constant inlet profile and turbulence model. For non-constant C_μ, instead of using Eq. (19) to calculate the σ_ε at each time step, the constant σ_ε value can be maintained while adding the following source term to the ε equation:

$$S_\varepsilon(z) = \frac{\rho u^{*4}}{(z + z_0)^2} \left(\frac{(C_2 - C_1)\sqrt{C_\mu}}{\kappa^2} - \frac{1}{\sigma_\varepsilon} \right) \tag{22}$$

Further, Parente et al. [42] derived a new consistent inlet profile for turbulent kinetic energy based on the assumption of local equilibrium between dissipation and production of turbulence, as

$$k(z) = C_1 \ln(z + z_0) + C_2 \tag{23}$$

The difference between Eq. (18) and Eq. (23) is that the first one needs the additional source term in the turbulent kinetic energy equation (Eq. (821)) to force equilibrium while the second one is derived based on equilibrium condition from the beginning and doesn't need any additional source. Both Yang et al. [39] and Parente et al. [42] proposed accurate profiles but requiring experimental data to fit the parameters C_1 and C_2 in Eq. (18,23). This is not always available especially for full-scale

simulations. For this case, a semi-empirical alternative provided by Brost and

Wyngaard [43] can be used.

$$\frac{\langle u'^2\rangle}{u^{*2}} = 5 - 4\frac{z}{h}; \; \frac{\langle v'^2\rangle}{v^{*2}} = 2 - \frac{z}{h}; \; \frac{\langle w'^2\rangle}{w^{*2}} = 1.7 - \frac{z}{h}; \tag{24}$$

where h is the ABL height, and it can be deduced for homogenous flow from Bechmann

[44] relation:

$$\frac{hf_c}{u^{*2}} \approx 0.33 \tag{25}$$

Then, the variation of turbulence kinetic energy for typical Coriolis parameter $f_c = 10^{-4}$ is

$$k(z) = \frac{1}{2}(\langle u'\rangle^2 + \langle v'\rangle^2 + \langle w'\rangle^2) = \frac{u^{*2}}{2}\left(8.7 - 6\frac{z}{h}\right) \tag{26}$$

Similar to what's done for the k-ε model, in this study we derived ABL k-ω

model and boundary conditions appropriate for simulating ABL flows. First, we derived

the ω inlet profile based on the velocity inlet profile proposed by Richards and Hoxey

[35]. To relate ω and velocity, we substituted $\mu_t = \rho k/\omega$ in Eq. (7) to get

$$\omega = \rho\frac{k}{\tau}\frac{\partial u}{\partial z} \tag{27}$$

For the case of homogenous ABL flow, turbulence generation $(\tau\partial u/\partial z)$ and

dissipation $(\beta^*\rho k\omega)$ are equal, then

$$\tau\frac{\partial u}{\partial z} = \beta^*\rho k\rho\frac{k}{\tau}\frac{\partial u}{\partial z} \; \Rightarrow \; k = \frac{u^{*2}}{\sqrt{\beta^*}} \tag{28}$$

17

After that, we substituted k and τ in Eq. (27) by $\left(u^{*2}/\sqrt{\beta^*}\right)$ and $\left(\rho u^{*2}\right)$ respectively,

and we used Eq. (11) to calculate $\partial u/\partial z$. Then, the ω inlet profile function of known

quantities become

$$\omega = \frac{u^*}{\sqrt{\beta^*}\kappa}\frac{1}{z+z_0} \tag{29}$$

The ω transport equation should be consistent with the inlet profile which means that

inlet ω profile should satisfy the ω equation. For two-dimensional, steady,

incompressible, homogenous ABL flow, the ω equation can be reduced to

$$\frac{\partial}{\partial z}\left[\left(\mu+\frac{\mu_t}{\sigma_\omega}\right)\frac{\partial\omega}{\partial z}\right] + \alpha\frac{\omega}{k}\tau\frac{\partial u}{\partial z} - \beta\rho\omega^2 + S_\omega = 0 \tag{30}$$

The terms of Eq. (30) are given by

$$\frac{\partial}{\partial z}\left[\left(\mu+\frac{\mu_t}{\sigma_\omega}\right)\frac{\partial\omega}{\partial z}\right] = \frac{\partial}{\partial z}\left[\left(\frac{\mu_t}{\sigma_\omega}\right)\frac{\partial\omega}{\partial z}\right] = \frac{\rho u^{*2}}{\sigma_\omega\sqrt{\beta^*}}\frac{1}{(z+z_0)^2}$$

$$\alpha\frac{\omega}{k}\tau\frac{\partial u}{\partial z} = \frac{\alpha\rho u^{*2}}{\kappa^2(z+z_0)^2} \tag{31}$$

$$\beta\rho\omega^2 = \frac{\beta\rho u^{*2}}{\beta^*\kappa^2(z+z_0)^2}$$

By substituting the terms of Eq. (31) in Eq. (30) an extra source term for ω appears as

$$S_\omega = \frac{\rho u^{*2}}{(z+z_0)^2\sqrt{\beta^*}}\left[\frac{\beta-\alpha\beta^*}{\sqrt{\beta^*}\kappa^2}-\frac{1}{\sigma_\omega}\right] \tag{32}$$

18

The source term in Eq. (32) should be added to the ω equation to insure consistency between inlet profile and model. At the top of the domain, a specified flux boundary condition for ω is used and is given by

$$FluxT_\omega = \frac{\mu_t}{\sigma_\omega} \frac{\partial \omega}{\partial z} \qquad (33)$$

Using the ω inlet profile, the flux becomes

$$FluxT_\omega = \frac{\rho u^{*2}}{\sqrt{\beta^*} \sigma_\omega (z + z_0)} \qquad (34)$$

ABL domains are generally divided into three regions that are the central region where objects are modeled explicitly and upstream and downstream regions where objects are modeled implicitly by taking their effect on flow as roughness. Usually for rough surfaces, a modified wall functions based on sand grain roughness are used

$$U^+ = \frac{1}{\kappa} log(Ey^+) - \Delta B \qquad (35)$$

where $U^+ = u_p u^* / \tau_w / \rho$; $y^+ = \rho u^* y_p / \mu$; E is an integration constant; and u^* is the frictional velocity. ΔB represents the departure from smooth conditions, and it can be calculated according to Cebeci and Bradshaw [36] depending on sand grain roughness as

$$\Delta B = 0 \quad K_s^+ < 2.25$$

$$\Delta B = \frac{1}{\kappa} log\left(\frac{K_s^+ - 2.25}{87.75} + C_s K_s^+\right) sin(0.4258[log K_s^+ - 0.811]) \qquad (36)$$

$$2.25 < K_s^+ < 90$$

$$\Delta B = \frac{1}{\kappa} log(1 + C_s K_s^+) \quad K_s^+ > 90$$

However, Blocken et al. [38] proved that using K_s-type wall functions can't achieve horizontally homogeneous ABL flow without some errors and mentioned some remedial measures to rectify errors. On the other hand, Parente et al. [40] developed a new wall function based on aerodynamic length to overcome K_s-type wall functions limitations. Parente et al. [40] wall function is a reformulation of Richards and Hoxey [35] except that $G_k = \tau_w^2 / \rho \kappa C_\mu^{0.25} k^{0.5}(z_p + z_0)$ is calculated at cell centroid instead of integrating it over the first cell height length to avoid the well documented peak production of turbulent kinetic energy at the wall [45]. The new wall function preserve the universal from $u = (u_*/\kappa)\ln(E'z^{+\prime})$, where E' and $z^{+\prime}$ are defined as

$$E' = \begin{cases} E & \text{smooth} \\ \dfrac{\nu}{z_0 u^*} & \text{rough} \end{cases} \qquad z^{+\prime} = \begin{cases} \dfrac{z_p u^*}{\nu} & \text{smooth} \\ \dfrac{(z_p + z_0)u^*}{\nu} & \text{rough} \end{cases} \qquad (37)$$

The frictional velocity in Eq. (37) is variable and is calculated as $u^* = C_\mu^{0.25} k_p^{0.5}$. The new wall function formulation improves standard approach while preserving its flexibility. We altered between rough and smooth modes based on roughness properties of wall surfaces.

The new k-ε formulation is valid when the ABL is undisturbed. Thus, in the building influence area where buildings are modeled using their real shapes, the standard model should be used. To detect the building influence area automatically, and to provide smooth transition and blending between the implicit and explicit regions, we

used a method based on the local deviation from the undisturbed ABL conditions [42].

The deviation can be calculated by pure or hybrid blending as shown in Table 1 [46].

Table 1 Calculation of the deviation for explicit-implicit blending

Pure Blending		Hybrid Blending
Based on V	Based on TKE	V and TKE
$\delta_u = min\left[\left\|\dfrac{u - u_{ABL}}{u_{ABL}}\right\|, 1\right]$	$\delta_k = min\left[\left\|\dfrac{k - k_{ABL}}{k_{ABL}}\right\|, 1\right]$	$\delta_h = max[\delta_u, \delta_k]$

The additional source terms of the k and ε equations and the $C\mu$ parameter are

then weighted as a function of δ to allow smooth transition between explicit and

implicit regions. Two formulations for the transition between the different flow regions

are available, and they are the polynomial (Eq. (40)) and the sinusoidal functions (Eq.

(41)).

$$\emptyset = \emptyset_{std} + (1 - \delta^\alpha)(\emptyset_{hom} - \emptyset_{std}) \tag{38}$$

$$\emptyset = \emptyset_{std} + (\emptyset_{ABL} - \emptyset_{std})\left[1 - 0.5\left(1 + sin(\delta^*)\right)\right]^\alpha$$
$$\delta^* = \pi\max(\delta - 0.5, -0.5) \tag{39}$$

In summary, consistent model for neutral stratification condition can be obtained

by using Eq. (10) for the u inlet profile, any of Eq. (12),(18),(23), or (26) for the k inlet

profile, Eq. (13) for the ε inlet profile when using the $k - \varepsilon$ model, and Eq. (29) for the

ω inlet profile when using the $k - \omega$ model. The source term given by Eq. (21) should

be added to the k equation when using Eq. (18) or Eq. (23) as inlet profiles for k. The

source term displayed in Eq. (22) should be added to the ε equation, and the source term

in Eq. (32) should be added to the ω equation. The full set of inlet conditions and source

terms are summarized in Table 2. Hybrid or pure blending can be used to calculate δ,

and either Eq. (38) or Eq. (39) can be used to transit between implicit and explicit regions. Equation (37) can be used for wall functions instead of the standard rough wall functions.

Table 2 Summary of inlet conditions and turbulence model additional source terms

Variable	Equation	Additional Source
$u(z)$	Eqn. (10)	0
$k(z)$	a) Eqn. (12)	0
	b) Eqn. (18)	Eqn. (21)
	c) Eqn. (23)	0
	d) Eqn. (26)	Eqn. (21)
$\varepsilon(z)$	Eqn. (13)	Eqn. (22)
$\omega(z)$	Eqn. (29)	Eqn. (32)

D. Dispersion Models

In the Lagrangian model, we represented pollutants or gases by group of particles to simulate their distribution in the domain. Particles' dispersion and the concentration field are calculated by dividing the effects of advection and diffusion into separate passive steps. The position of each particle is calculated by solving the advection equation while the effect of the particle on the concentration field is calculated by the diffusion equation.

We integrated the Lagrangian form of Newton's second law applied on a particle to get the advection equation (Eq. (40)).

$$m_p \frac{d\boldsymbol{U}_p}{dt} = \boldsymbol{F}_{Drag} + \boldsymbol{F}_{bouancy} + \boldsymbol{F}_{others}$$

$$m_p \frac{d\boldsymbol{U}_p}{dt} = \frac{1}{2}\rho_f C_D |\boldsymbol{U} - \boldsymbol{U}_p|(\boldsymbol{U} - \boldsymbol{U}_p)A_p + (\rho_p - \rho_s)\boldsymbol{g}V_p + \boldsymbol{F}_{others}$$

(40)

Then, the sequence of events for advecting the particle is summarized as

1. Calculate Reynolds number R_e using $\boldsymbol{U}_p$ from previous time step

$$R_e = \frac{\rho d_p |\boldsymbol{U} - \boldsymbol{U}_p|}{\mu} \tag{41}$$

2. Calculate the drag coefficient C_D

$$C_D = \begin{cases} \dfrac{24}{R_e}\left(1 + 0.15R_e^{0.687}\right) & R_e < 1000 \\ 0.44 & R_e > 1000 \end{cases} \tag{42}$$

3. Solve the force balance to calculate $\boldsymbol{U}_p$ after writing it in this form

$$\frac{d\boldsymbol{U}_p}{dt} = \tau_p\left(\boldsymbol{U} - \boldsymbol{U}_p\right) + \alpha_p \tag{43}$$

4. Update the particle position by solving the trajectory equation

$$\frac{d\boldsymbol{x}_p}{dt} = \boldsymbol{U}_p \tag{44}$$

For solving the force balance and the trajectory equations the following schemes were implemented: the Euler implicit, the Euler explicit, the second order Runge-Kutta, the fourth order Runge-Kutta, and two trapezoidal numerical discretization schemes, and one analytical method based on the analytical solution of the force balance equation.

To get the diffusion equation, Fick's law of diffusion [47] was solved using the "product rule" for the case of a particle spreading in all directions without being restricted by boundaries [48]. The equation describes how a particle of mass M deposit

at a point (x_0, y_0, z_0) at time $t = 0$ affects the concentration at point (x, y, z), and it can be written as

$$C(x, y, z, t) = \frac{M}{(4\pi t)^{\frac{3}{2}} (D_x D_y D_z)^{1/2}} \exp\left(-\frac{(x-x_0)^2}{4D_x t} - \frac{(y-y_0)^2}{4D_y t} - \frac{(z-z_0)^2}{4D_z t}\right) \quad (45)$$

where D_x, D_y and D_z are the diffusivities in x, y and z directions. If the diffusivity is isotropic, and by defining the core-radius to be $\sigma_{(t)}^2 = 4Dt$, the equation becomes

$$C(x, y, z, t) = \frac{M}{\pi^{3/2} \sigma_{(t)}^3} \exp\left(-\frac{d^2}{\sigma_{(t)}^2}\right) \quad (46)$$

$$\sigma_{(t)} = \sqrt{\sigma_{(t-1)}^2 + 4Ddt} \quad (47)$$

In simulations, concentration field is described by a number of particles, and the effect of all particles on each cell centroid is calculated by superposing the effects of particles according to

$$C(x, y, z, t) = \sum_{i=1}^{nParticles} \frac{M_i}{\pi^{3/2} \sigma_{(i,t)}^3} \exp\left(-\frac{d_i^2}{\sigma_{(i,t)}^2}\right) \quad (48)$$

On the other hand, we calculated the concentration in the Eulerian model by solving the concentration transport equation that we discretized using the finite volume method.

$$\frac{\partial c}{\partial t} + \nabla \cdot (\mathbf{v}c) = \nabla \cdot [D\nabla c] + S_c \quad (49)$$

24

where c is the concentration, $\mathbf{v}$ is the wind velocity, D is the effective diffusion coefficient, S_c is the source term that can represent source or sink of concentration. The effective diffusivity D is the sum of the molecular and eddy diffusivities, and the eddy diffusivity is defined by

$$D_t = \frac{v_t}{Sc_t} \tag{50}$$

where Sc_t is the Schmidt number and it has an optimum value between 0.2 and 1.3 [49].

CHAPTER II

MODEL VALIDATION AND CONCLUSION

A. Test Cases

To validate the wind field model, first we simulated the CEDVAL A1 [50] wind tunnel experiment in the absence of obstacles to test the sustainability of ABL velocity and turbulence inlet profiles. The sustainability of the model is tested by showing that the inlet profiles are unchanged through an empty domain. Then, we simulated the flow and particles dispersion in the presence of a single building for CEDVAL A1 test case. After that, our model is further validated by simulating the more challenging CEDVAL B1 test case dealing with an array of buildings.

1. CEDVAL A1 empty domain

We carried out the numerical simulations for empty CEDVAL A1 domain using the k-ε and k-ω models, standard and modified wall functions, and the four different k inlet profiles listed in Table 2 to note differences between the cases. For inlet boundary conditions, we used the inlet profiles listed in Table 2 for $u, \varepsilon,$ and ω. For the top patch and for the outlet section, we applied a retarding shear stress and a pressure outlet respectively as recommended by Richards and Hoxey [35]. The empty domain is simulated using a two-dimensional domain 4 m in length 1 m in height. The computational grid is uniform in the horizontal direction and stretched in the vertical direction such that the first cell height z_p is 2.5e-3 m with a total number of 400×71 cells. The aerodynamic roughness z_0 is set at 0.00075 m, and we calculated the equivalent sand grain roughness K_s and the roughness constant C_s for standard rough

wall functions based on the equations mentioned by Blocken et al. [38] that we listed in

Table 3. CEDVAL A1 domain is well described in terms of velocity and turbulent

kinetic energy measurements that are used to calculate the model parameters listed in

Table 3.

Table 3 Velocity and turbulent kinetic energy model parameters

u^*		$0.347 \ ms^{-1}$
z_0		$0.00075 \ m$
$C_s = E z_0 / z_p$		$K_s = 30 z_p$
Eqn. (18) parameters	C_1	-0.0628
	C_2	0.2186
Eqn. (26) parameters	C_1	-0.0579
	C_2	0.4706

2. *Full scale empty domain*

The ability of the model with the new wall function formulation to maintain inlet

profiles throughout an empty full-scale domain was tested by simulating the Silsoe cube

test case [51]. The domain is 5000 m length by 500 m height. We used the blockMesh

utility to create a 2D hexahedral grid that is uniform in the longitudinal direction and

stretched vertically such that the first cell height is 1m. We used the same boundary

conditions used in the wind tunnel empty domain test case, and we tested the model

with the four TKE inlet profiles given in Eq. (12,18,23,26). Also, we used both the ABL

$k - \varepsilon$ and $k - \omega$ models with the new wall function formulation. However, inlet profile

is not a big deal in this test case since the aim here is only to test the sustainability and

not to compare with experimental data. Thus, we used arbitrary parameters for TKE

profiles when using Eqn. (18) and Eqn. (23). We got the velocity inlet profile from the
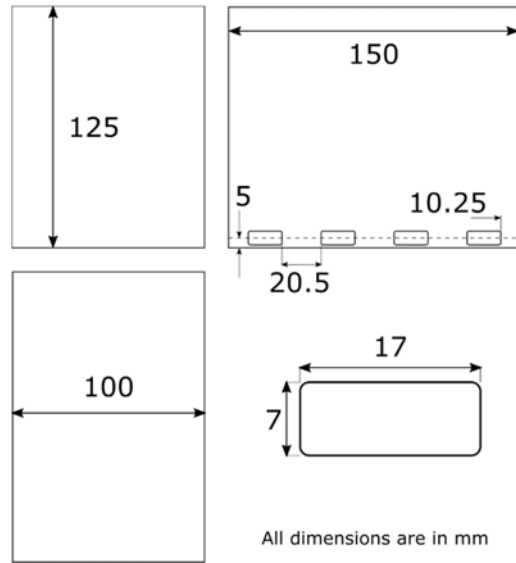
blind test exercise data [51].

Figure 1 CEDVAL test cases building geometry and dimensions

3. CEDVAL A1 single building

We simulated the CEDVAL A1 test case in the presence of single building using

the *k-ε ABL, k-ω ABL*, and *k-ω SST* models to validate their abilities in solving and

transitioning between homogenous and perturbed ABL flow. Then, we used the

obtained flow fields to run the dispersion model and compare it with the concentration

data of the experiment. The geometry of the building is shown in Figure 1, its length,

height, and width are 100 mm, 125mm, and 150mm respectively. It has four sources of

tracer gas that represent emissions from underground parking garage located near the

ground in the leeward direction of the building. The center of the bottom face of the

building is taken to be the origin of the Cartesian system, x-axis is pointing downstream

and z-axis is pointing upward. The wind direction is in the longitudinal direction of the

grid, and it creates a symmetrical wind field with respect to the $(y = 0)$ plane, so only

half the domain is considered as shown in Figure 2b. The inlet and outlet of the domain

are located 1m upstream and 3m downstream of the building's center respectively. We

28

generated two hexahedral meshes one for *k-ε ABL* and *k-ω ABL* models, and the other for *k-ω SST* model using the OpenFoam blockMesh utility. The domain was divided into several blocks where each of them has its number of divisions and expansion ratio. This helped in obtaining acceptable number of cells while ensuring that near-wall cell length is small enough.

For the *k-ε ABL* and *k-ω ABL* models we used the new wall function formulation (Eq. (37)) with first near wall cell length equal to 7e-4 m and a mesh of 2.2 million cells. For the inlet patch we used Eq. (10) for *u*, Eq. (23) for *k*, Eq. (13) for *ε* when using the *k-ε ABL* model, and Eq. (29) for *ω* when using the *k-ω ABL* model. For the top patch we used a retarding shear stress, for the *y=0* plane we applied symmetry boundary condition, for the side patch we applied wall-slip condition, and for the outlet patch we specified the pressure. We used the sinusoidal blending function (Eq. 39) with *α=4* and deviation being calculated according to velocity to blend between explicit and implicit regions. For the *k-ω SST* model, we solved all the way to the wall without using wall functions, so we used a finer mesh that has six million cells with the first near wall cell length equal to 5e-5 m. For the inlet patch, we used Eq. (10) for *u*, Eq. (12) for *k*, and Eq. (29) for *ω*. At the walls we specified $u = 0, k = 0, and\ \omega = 60v/0.075y^2$, and for the rest of the patches we used the same boundary conditions used for the *k-ε ABL* and *k-ω ABL* simulations. Measurements of wind flow are available within two sampling planes: $y = 0$ (603 points) and $z = 0.035m$ (643 points), and they are published in the CEDVAL A1-1 data base. For the gas source inlets, we specified the values as follows

$$u = 0.024; \ k = 1.5(ul)^2$$
$$\varepsilon = C_\mu^{0.75} k^{1.5}/l; \ \omega = k^{0.5}/(C_\mu^{0.25} l) \qquad (51)$$
$$l = 0.075 l_{source}$$

Concentration measurements are available on six planes: $x = 0.051m, y = 0, y = -0.06m, y = -0.076m, z = 0.01m,$ and $z = 0.035m$, and they are published in CEDVAL A1_5 data in dimensionless form

$$k = \frac{C_{measure}}{C_{source}} \frac{u_{ref} H^2}{Q_{source}} \tag{52}$$

where C_{source} is the tracer gas concentration at the source, u_{ref} is the reference speed at the reference height 0.66m, H is the building height, and Q_{source} is the flow rate of the tracer gas at the source.

Choosing inputs for the Lagrangian model is of vital importance to obtain a correct solution. For that, we chose small enough initial core-radii to describe sources shapes accurately, big enough number of particles per source to insure special smoothness of concentration field, small enough time step size to insure semi continues particles trajectories and concentration field by considering the core-radii and the velocities of particles, and big enough number of time steps to insure that all the particles emitted at the beginning of the simulation passed out the domain. Accordingly, we chose the particles' core-radii to be equal to 5e-4m with 700 particles per source, and a time step size equal to 2.5e-4s with 6000 time steps. We used the fourth order Runge-Kutta scheme for advection, and a Schmidt number *Sc_t = 0.4* for eddy diffusion calculation. We assumed perfect reflection for particles when hitting walls or symmetry patches. The buildings and ground are considered walls, the *y=0* plane is considered symmetry, and all other boundaries are considered opened boundaries in the Lagrangian model.

4. CEDVAL B1 array of buildings

We simulated the flow around an array of buildings to validate our model over more complex geometry. The buildings have the same geometry of the CEDVAL A1 building test case, and they are seven in the longitudinal direction by three in the transverse direction as shown in Figure 2-b. The center of the bottom face of the blue building is the origin of the domain, the z-axis points upward and the x-axis in the wind direction. The inlet of the domain is located 1.85m upstream of this building or 1m upstream of the first building in the array, and the outlet of the domain is located 4.45m downstream of the blue building. The dimensions of the domain are the same as the wind tunnel dimensions and they are 1m high and 1.5m wide. Similar to what's done for the single building case, we generated hexahedral mesh using blockMesh OpenFoam utility based on dividing the domain into several blocks. The near-wall cells heights are 7e-4 m, the resolution near building influence area is 5e-3m, and the total number of cells is 3.5 million cells. We simulated the case using both *k-ε ABL* and *k-ω ABL* models with the same boundary conditions used for the single building case.
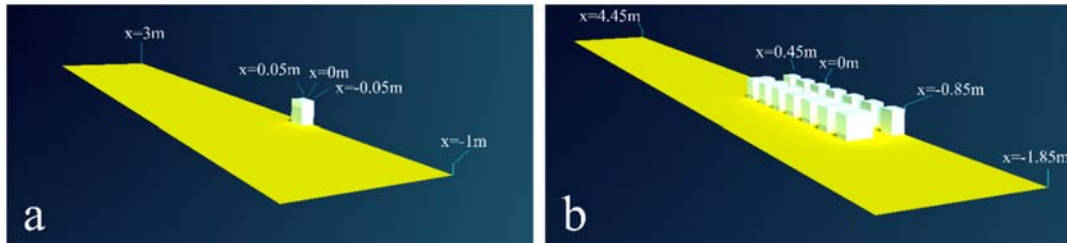

Figure 2 Test Cases CEDVAL A1 (a) and CEDVAL B1 (b) domains

B. Validation Metrics

We quantified the agreement between model and measured results based on the metrics recommended by the COST guideline that are accepted for our work [52]. We

used the hit rate, FAC2, MG metrics for the velocity components and the FAC2, FB, and MG metrics for the concentration. The hit rate expression is as follows:

$$q = \frac{1}{n}\sum_{i=1}^{n} N_i \tag{53}$$

with

$$N_i = \begin{cases} 1 \text{ if } \left| \dfrac{P_i - E_i}{E_i} \right| \leq \delta_r \text{ or } |P_i - E_i| \leq \delta_a \\ 0 \qquad\qquad\qquad else \end{cases} \tag{54}$$

Where q is the hit rate, n is the number of measurement points, and P_i is the predicted value of the experimental value E_i at a location i. δ_r is the relative uncertainty and it describes the allowed fractional deviation. It is the sum of the allowed imprecision of simulation results and the reproducibility of wind tunnel measurements, and its value is 0.25 for our case. δ_a is the repeatability, and it represent the allowed absolute deviation. δ_a is 0.06 for the velocity components [53-55], whereas for normalized concentration k, it is given as a function of its measured value by the power law $1.09k^{0.63}$ with additional criteria, k of 0.083 to avoid zero value near k equal zero [56].

FAC2 is similar to hit rate and it is the ratio of CFD predictions that are within a factor of two of the experimental data. It is defined as

$$FAC2 = \frac{1}{n}\sum_{i=1}^{n} N_i \tag{55}$$

with

$$N_i = \begin{cases} 1 & if\ 0.5 \le \dfrac{P_i}{N_i} \le 2.0 \\ 1 & if\ P_i \le \delta_a\ and\ E_i \le \delta_a \\ 0 & else \end{cases} \qquad (56)$$

The geometric mean bias (MG) represents systematic errors by measuring the mean bias logarithmically, so it can be used for vectors and scalars and it is given by

$$MG = \exp(\overline{\ln E'} - \overline{\ln P'}) \qquad (57)$$

with

$$E_i' = \max(\delta_a, E_i)\ and\ P_i' = \max(\delta_a, P_i) \qquad (58)$$

To decide whether the model is accepted or not according to the validation metrics, limits should be specified. The German VDI guideline [55] requires $q \ge 0.66$ for all velocity components. Several studies used FAC2 ≥ 0.5 and $0.7 \le MG \le 1.3$ [53, 57].
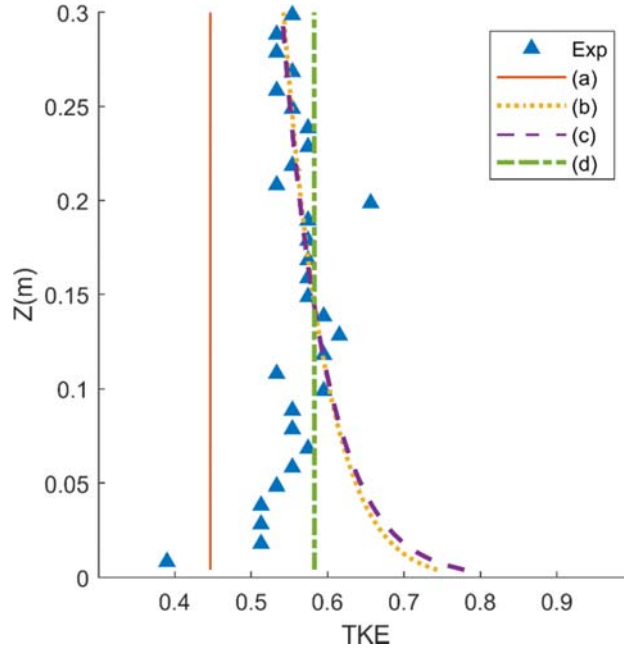
C. Results

1. CEDVAL A1 empty domain

Figure 3 Comparison of experimental data with different inlet conditions for turbulent kinetic energy given by (a) Eqn. (12), (b) Eqn. (18), (c) Eqn. (23), and (d) Eqn. (26)

Figure 3 shows a comparison between turbulent kinetic energy inlet profiles and the experimental data available at the inlet. Constant profile (a) (Eq. (12)) doesn't describe the experimental data while the variable profiles (b) (Eq. (18)) and (c) (Eq. (23)) shows the best fit. However, the profiles (b) and (c) require experimental data to calculate their fitting parameters C_1 and C_2, so it is accepted to use profile (d) (Eq. 26) when there is no available data at inlet since this profile is also close to experimental data.

Figure 4 shows turbulent kinetic energy, velocity, turbulence dissipation rate, and the specific turbulence dissipation profiles at inlet and outlet sections for 16 empty domain simulations. We tested in the simulations the use of the different turbulent kinetic energy inlet profiles listed in Table 2 (Eq. (12), (18), (23), and (26)), the use of

standard k_s type (Eq. (35)) and modified ABL wall functions (Eq. (37)), and the use of

modified k-ε and k-ω ABL models. For a homogenous ABL flow, it is not the intention

to test the development of flow variables. Thus, for empty domain, the best approach is

the one that maintain inlet profiles at the outlet section. Although we used the

recommended value for $C_s = E z_0 / z_p$ when using the standard wall function, it only

helped in maintaining the velocity, the dissipation, and the specific dissipation profiles,

but error still occur in the turbulent kinetic energy profile. The use of standard wall

function with the k-ε ABL model result in overestimating TKE when using profile (a)

for TKE, and underestimation near the wall when using profiles (b), (c) and (d). Also,

when using the standard wall function with the k-ω ABL model it results in

underestimating TKE when using profiles (b), (c) and (d) for TKE. However, the use of

the new wall function formulation that is based on aerodynamic roughness, solved this

issue and maintained all flow variables. Thus, any of the 4 turbulent kinetic energy

profiles can be used with the k-ε or k-ω ABL models on condition that they are used

with the new wall function formulation and all flow variables will be maintained
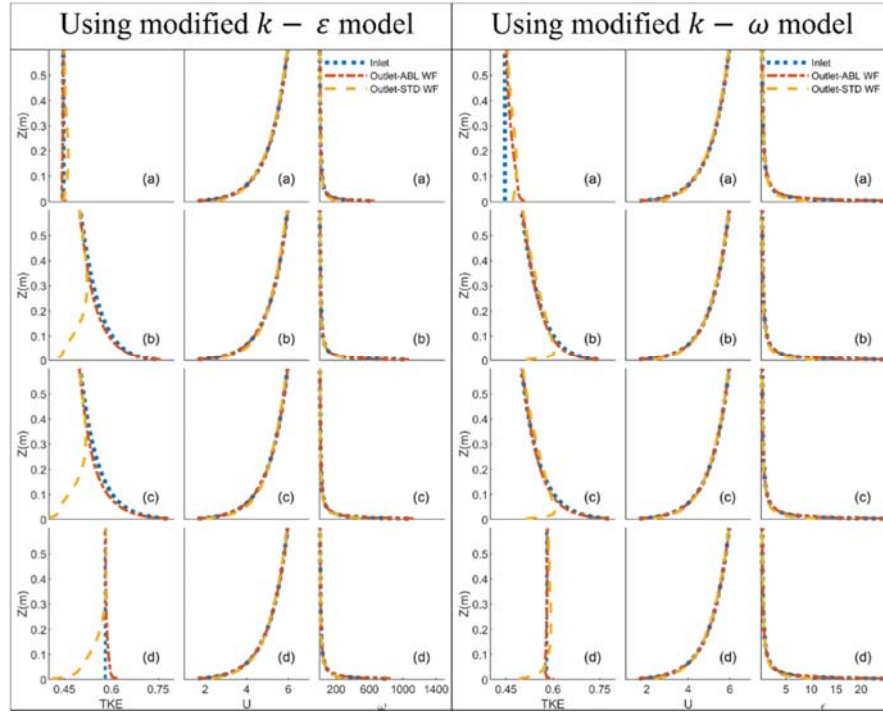
through the domain.

Figure 4 Inlet and outlet turbulent kinetic energy, velocity, and turbulence dissipation rate profiles when applying different inlet conditions for turbulent kinetic energy given by (a) Eqn. (12), (b) Eqn. (18), (c) Eqn. (23), and (d) Eqn. (26), and using the standard and ABL wall function formulation
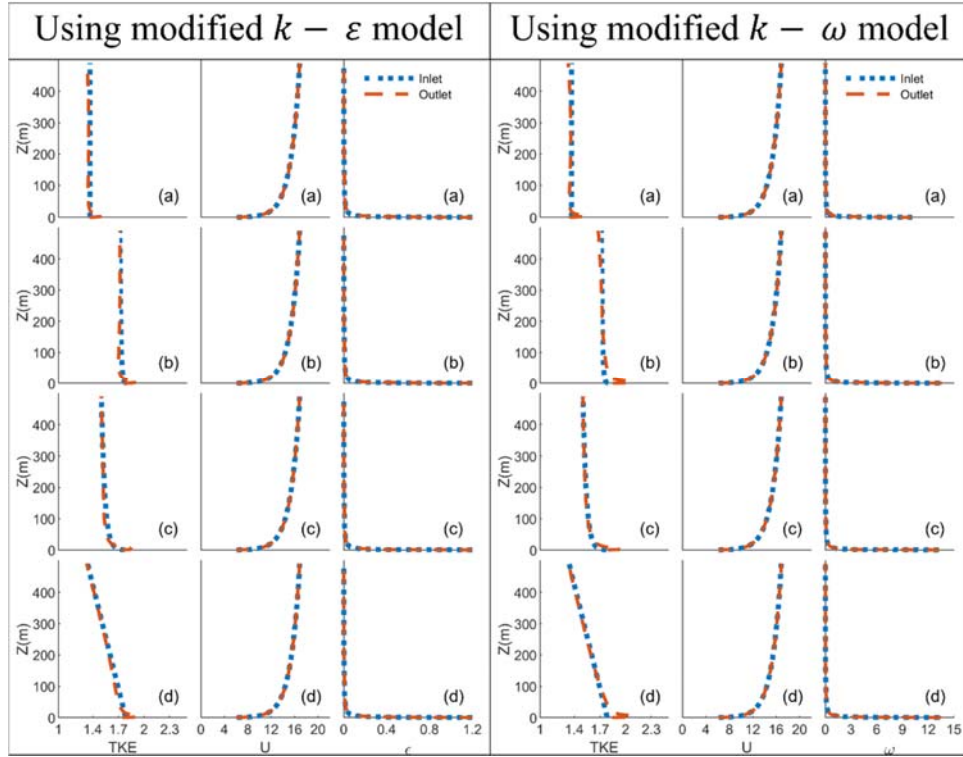
2. Full scale empty domain

Figure 5 Inlet and outlet turbulent kinetic energy, velocity, turbulence dissipation rate, and specific dissipation profiles when applying different inlet conditions for turbulent kinetic energy given by (a) Eqn. (12), (b) Eqn. (18), (c) Eqn. (23), and (d) Eqn. (26)

Figure 4 shows inlet and outlet profiles for the turbulent kinetic energy, the velocity, the turbulent dissipation rate, and specific dissipation for the full-scale empty domain case when using the modified k-ε and the k-ω model with the four turbulent kinetic energy profiles given by Eqns. (12,18,23,26). Similar to the CEDVAL A1 test case, we concluded that the modified k-ε and the k-ω model with the new wall function formulation can be successfully used to simulate ABL flow while maintaining the inlet profiles in the absence of obstacles for full scale domains.
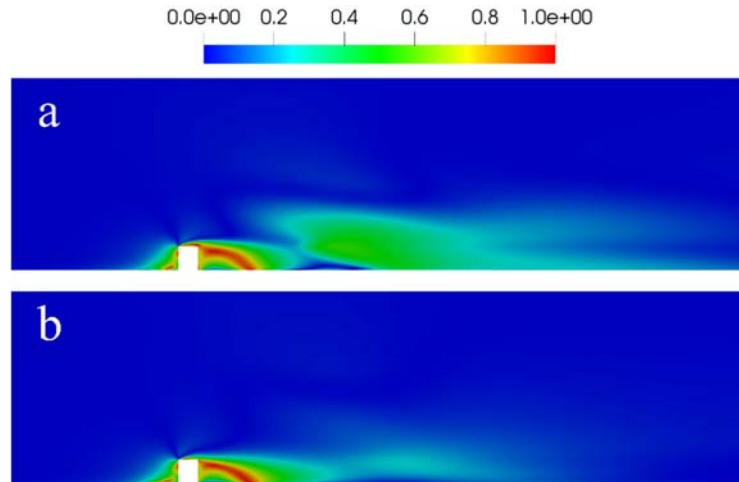
3. CEDVAL A1 single building

Figure 6 Blending factor for the case of single building when using k-ε model (a) and k-ω model (b) at the symmetry plane

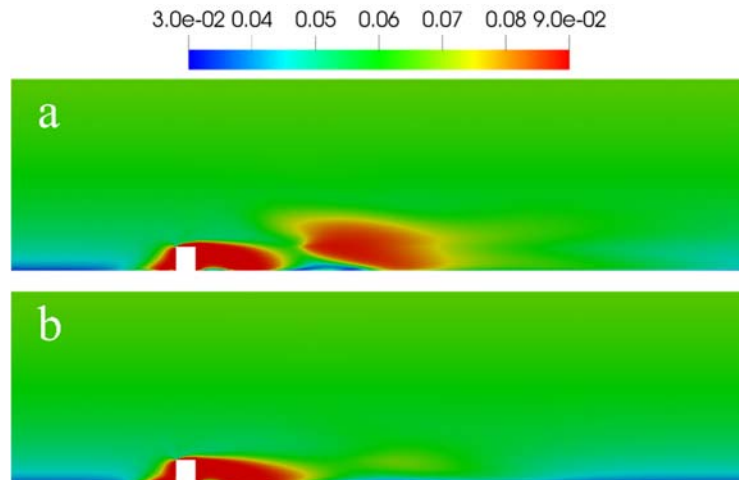Figure 7 Cμ for the case of single building when using k-ε model (a) and k-ω model (b) at the symmetry plane

Figure 6.a and Figure 6.b shows contour plots for the blending factor at the symmetry plane using the k-ε and k-ω models respectively. We can note from the figure that the building influence area for both cases is not a spherical shape around the building as the old models that are based on prescribing this area were assuming. Also, we can notice that this method works better with the k-ω model than with the k-ε model since blending factor in Figure 6.a show high values in a region far from the building.

Figure 7.a and Figure 7.b shows contour plots for C_μ at the symmetry plane using the *k-ε* and *k-ω* models respectively. The values of C_μ are in line with the blending factor values. This give a sign that the method is working properly since the values of C_μ are in-between ABL model value and the standard value based on the blending factor, blending parameter and blending equation used.

Figure 8 and Figure 9 show a comparison between experimental and numerical velocity and turbulent kinetic energy profiles at different locations in the domain using the *k-ε*, *k-ω* and *k-ω SST* models. We can notice from the figures that the velocity and turbulent kinetic energy profiles using *k-ε* and *k-ω* models are closer to the experimental measurements than the ones using the *k-ω SST*. This shows the advantage of using the new *k-ε* and *k-ω* models settings that are using a variable turbulent kinetic energy inlet profiles, rough wall functions based on aerodynamic roughness on rough surfaces, variable turbulent kinetic energy inlet profiles and automatic blending functions for building influence area detection with a modified models outside this area.
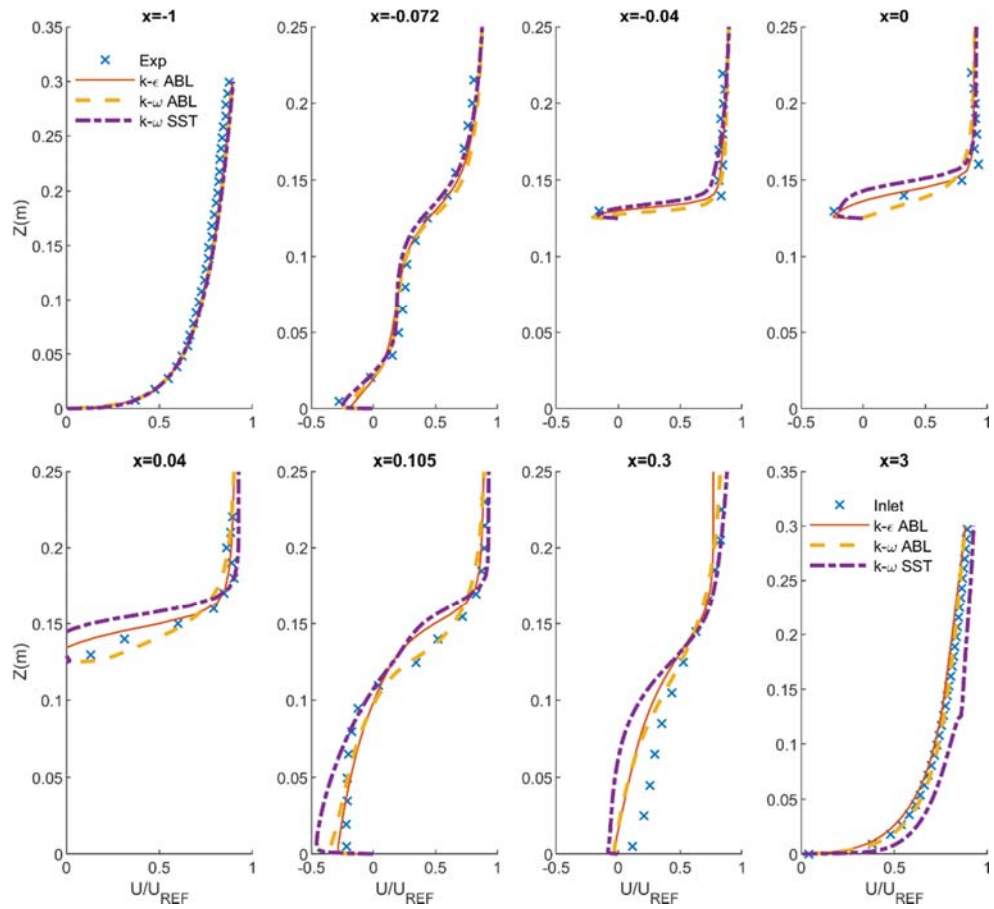
Figure 8 Comparison of experimental data and CFD simulations results for u-velocity
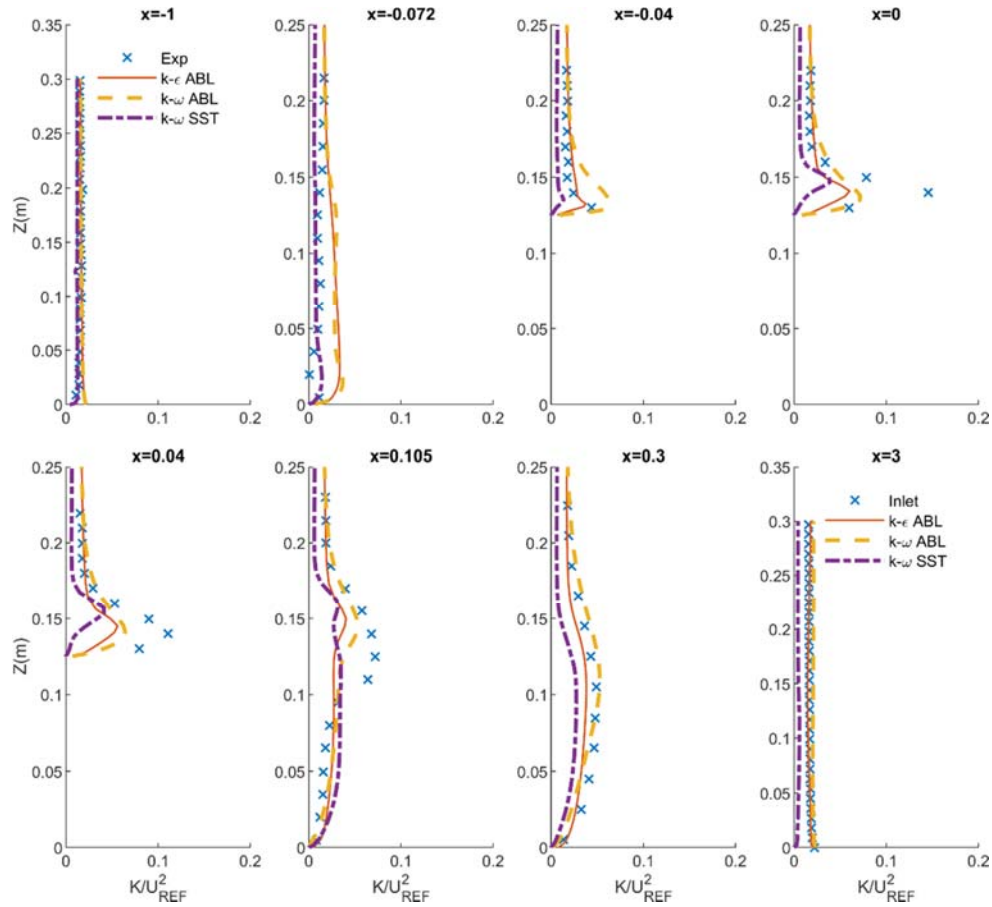components at different x positions in the y=0 plane

Figure 9 Comparison of experimental data and CFD simulations results for turbulent kinetic energy at different x positions in the y=0 plane

Table 4, Table 5 and Table 6 shows the validation metrics for normalized velocity components using the *k-ε*, *k-ω* and *k-ω SST* models respectively. According to these tables, the three models succeed in simulating the flow, however the *k-ω* model have the best metrics, then the *k-ε* model comes after it, and it is slightly better than the *k-ω SST* model. These results insures the results concluded from the velocity and turbulent kinetic energy profiles.

Table 4 Summary of velocity validation metrics when using k-ε model for single building case

Parameter	u/u_{ref}	v/u_{ref}	w/u_{ref}
Hit rate (≥ 0.66)	0.6665	0.7636	0.9303
FAC2 (≥ 0.5)	0.8443	0.9175	0.9850
MG ($0.7 - 1.3$)	1.2094	0.9236	0.9754

Table 5 Summary of velocity validation metrics when using k-ω model for single building case

Parameter	u/u_{ref}	v/u_{ref}	w/u_{ref}
Hit rate (≥ 0.66)	0.7199	0.8709	0.9452
FAC2 (≥ 0.5)	0.8788	0.9626	0.9801
MG ($0.7 - 1.3$)	1.1941	0.9576	1.0074

Table 6 Summary of velocity validation metrics when using k-ωSST model for single building case

Parameter	u/u_{ref}	v/u_{ref}	w/u_{ref}
Hit rate (≥ 0.66)	0.6773	0.7309	0.7993
FAC2 (≥ 0.5)	0.8515	0.9191	0.9038
MG ($0.7 - 1.3$)	1.2264	0.9543	0.9147

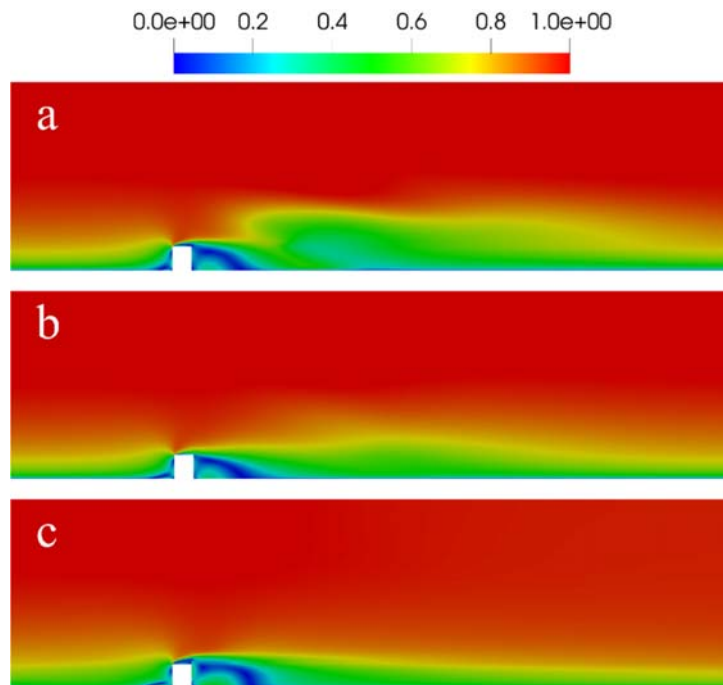
Figure 10 Velocity magnitude for the case of single building when using (a) the k- ε model, (b) the k- ω model and (c) the k- ω SST model.

Although the *k-ε* and the *k-ω* models were better in simulating the flow, the *k-ω*

SST model was better than both of them when simulating the dispersion of gas.

According to Table 7, the *k-ε* with Eulerian model for concentration failed in the FAC2

and MG validation tests while the k-ω barely succeeded in the FAC2 test, but also failed

in the MG validation test knowing the criteria for quality assurance are FAC2 ≥ 0.5 and

$0.7 \leq$ MG ≤ 1.3. On the other hand, the use k-ω *SST* with both Eulerian and Lagrangian

concentration models succeed in both the FAC2 and MG validation tests with close

FAC2 values. However, MG metric shows a positive bias when using the Eulerian

model and a negative bias when using the Lagrangian model, and this will be explained

through the discussion.

We used the k-ω *SST* model by solving all the way to the wall; for this, the mesh

for k-ω *SST* near walls is much finer than that for the k-ε and k-ω models that were used

with wall functions. This makes the k-ω *SST* model superior to other models in

predicting the velocity field in this region even though other models show better

validation metrics in the domain as a whole. At the same time, the gas sources are from

the bottom of the building, so they are largely affected by the velocity field near walls,

and this may be the cause why k-ω *SST* model succeed in predicting concentration field

unlike other models.

Figure 11 shows the vector field when using the k-ε, k-ω and k-ω *SST* models on

z=0.035m and y=0 planes, and Figure 10 shows the velocity magnitude when using the

three models. Although velocity magnitudes look close, the velocity vectors plot differ

from one model to other. Two parameters are important when comparing velocity

vectors in the building influence area that are the wake recirculation length (L_W) and the

rooftop reattachment length (L_R). The rooftop reattachment length appears in the y=0

xz-plane in Figure 11, and it represents the length that the fluid takes to reattach to the

ABL flow upcoming over the building. Where the wake recirculation length is the

length of recirculation in the leeward side of the building. We can see different sizes of

(L_R) and (L_W) lengths and different recirculation shapes between the used models and this have a significant effect on how the gas is advected.

This effect is noticed in Figure 12 that present the normalized concentration field using different models. In Figure 12.a where the k-ε with Eulerian concentration model is used, the biggest portion of the gas is advected to the windward side of the building before it recirculates and continues in the ABL flow direction. In Figure 12.b where the k-ω with Eulerian concentration model is used, the flow looks more diffusive since concentration don't follow strictly the wind field but it spreads around it. On the other hand, Figure 12.c that represents the concentration obtained by simulating flow using k-ωSST with Eulerian concentration model shows better results if we compared its shape with the experimental field shape that is available in the CEDVAL A1_5 data [50]. However, the k-ωSST with Lagrangian concentration model doesn't show an exact concentration distribution although it passed all the validation metrics.

Figure 13 investigates the difference between the Eulerian and Lagrangian models when dispersing a small group of particles and explains why the Lagrangian model results in an inaccurate contour plot for concentration. In Figure 13, when using the Eulerian model, the gas is diffused then the velocity field separates a group of particles from the bulk flow. Differently, when using the Lagrangian model the gas is diffused but the velocity field didn't separate the gas because all particles in this gas volume are represented by one particle and they are being advected by one velocity equal to the velocity of its center. Even if this volume was represented by more particles, all of them will follow similar trajectories because they will be initially very close to each other.

By referring to Figure 14 that shows the Lagrangian particles positions and core-radii, we can note that the particles are stuck in the recirculation zone for several loops

before they are out of the building influence area. Thus, the particle becomes totally

diffused when it is out of this area, and its effect on the concentration field becomes

very small. The diffusion can be noted from the particles' core-radii values far from the

building that are significantly larger than that near the building. A larger core-radius

means that the mass of the particle is spread in a larger volume which results in a less

effect on the concentration field and vise-versa.

Thus, when using the Lagrangian model, the concentration field follows strictly

the particles' trajectories, and the high concentration appears at the beginning of these

trajectories that are around the building. At the same time, CEDVAL A1_5 available

experimental data are mostly near the building, and this explains why the Lagrangian

MG metric has a negative bias that is an indicator that the predicted values are higher

than the experimental ones.

Table 7 Summary of validation metrics for normalized concentration in the single
building case when using different approaches

Flow Model	$k\text{-}\varepsilon$	$k\text{-}\omega$	$k\text{-}\omega$ SST	$k\text{-}\omega$ SST
Concentration model	Eulerian	Eulerian	Eulerian	Lagrangian
FAC2 (≥ 0.5)	0.40309	0.50081	0.68811	0.67345
MG ($0.7 - 1.3$)	0.40530	0.50230	1.19330	0.88460
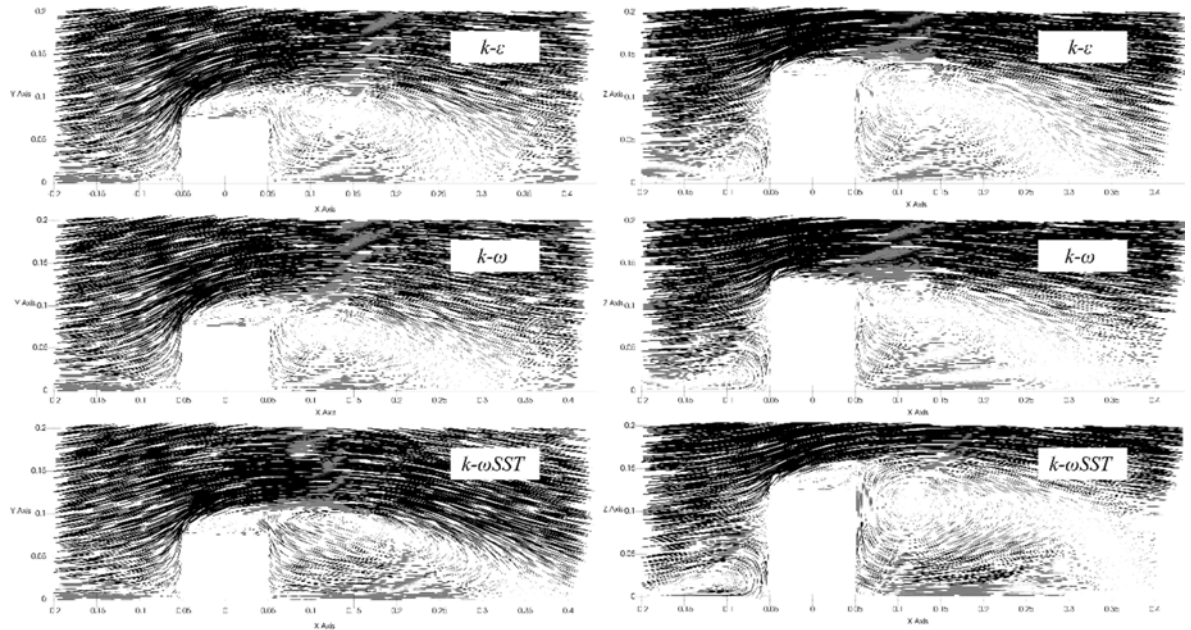
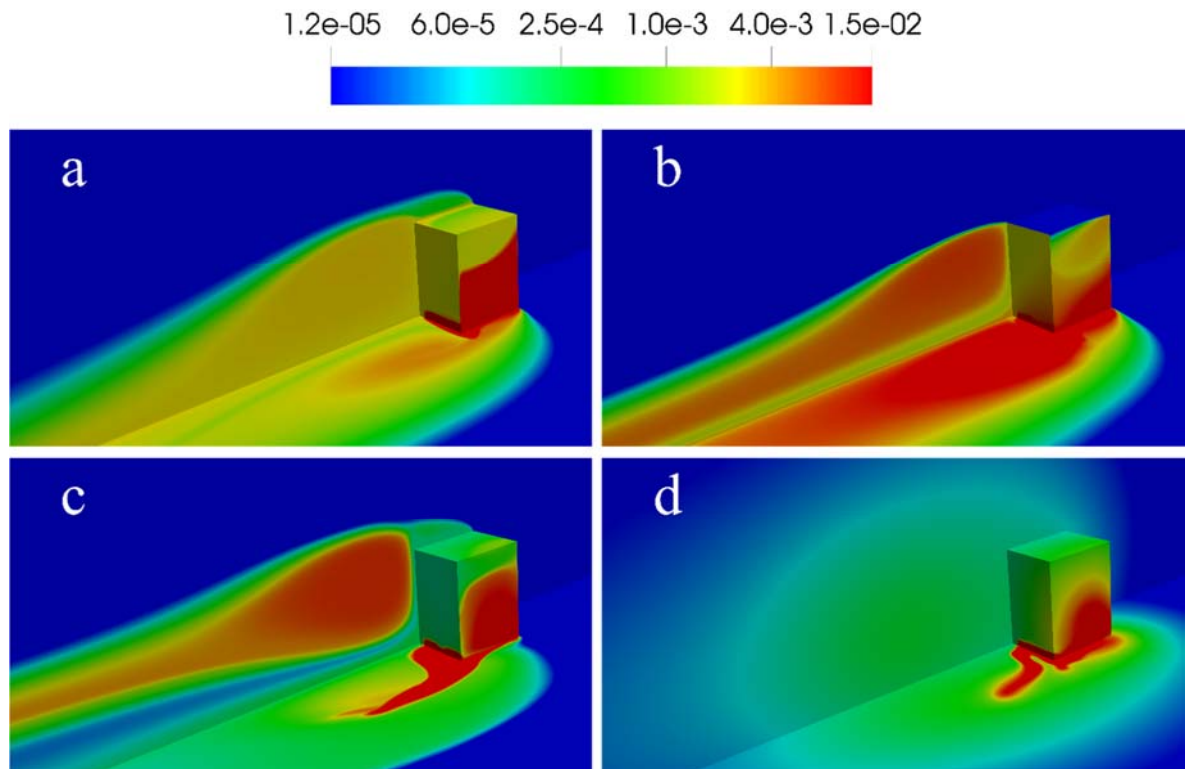Figure 11 Velocity vector plots of k-ε, k- ω and k- ω SST models on z=0.035m and y=0 planes

Figure 12 Normalized concentration for the case of single building when using (a) k- ε model with Eulerian concentration solver, (b) k- ω model with Eulerian concentration

solver, (c) k- ω SST model with Eulerian concentration solver and (d) k- ω SST model with Lagrangian concentration solver
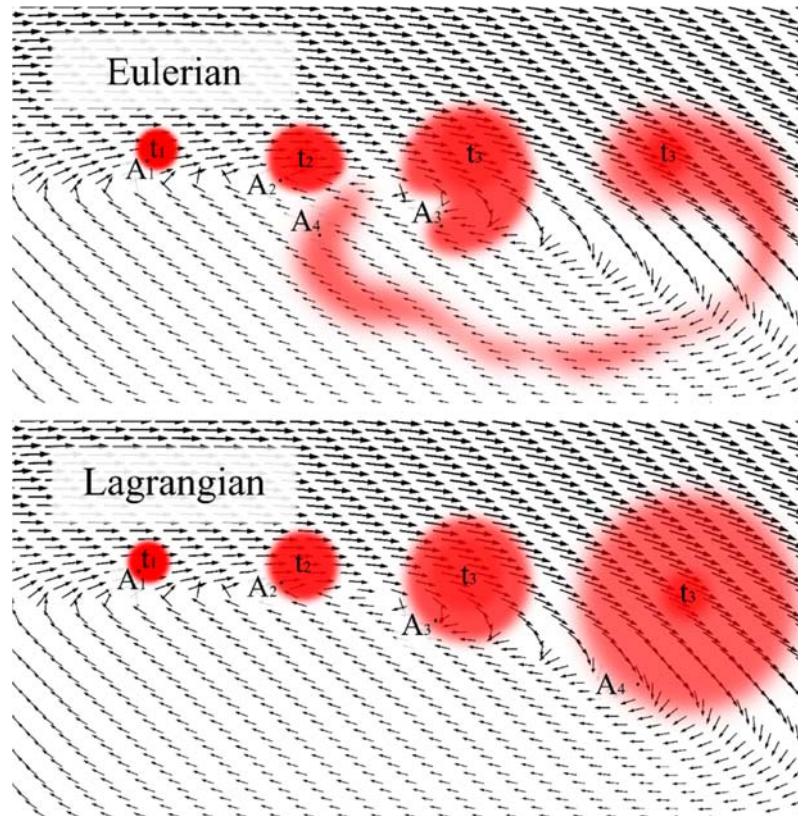

Figure 13 Comparison between Eulerian and Lagrangian models in dispersing group of particles
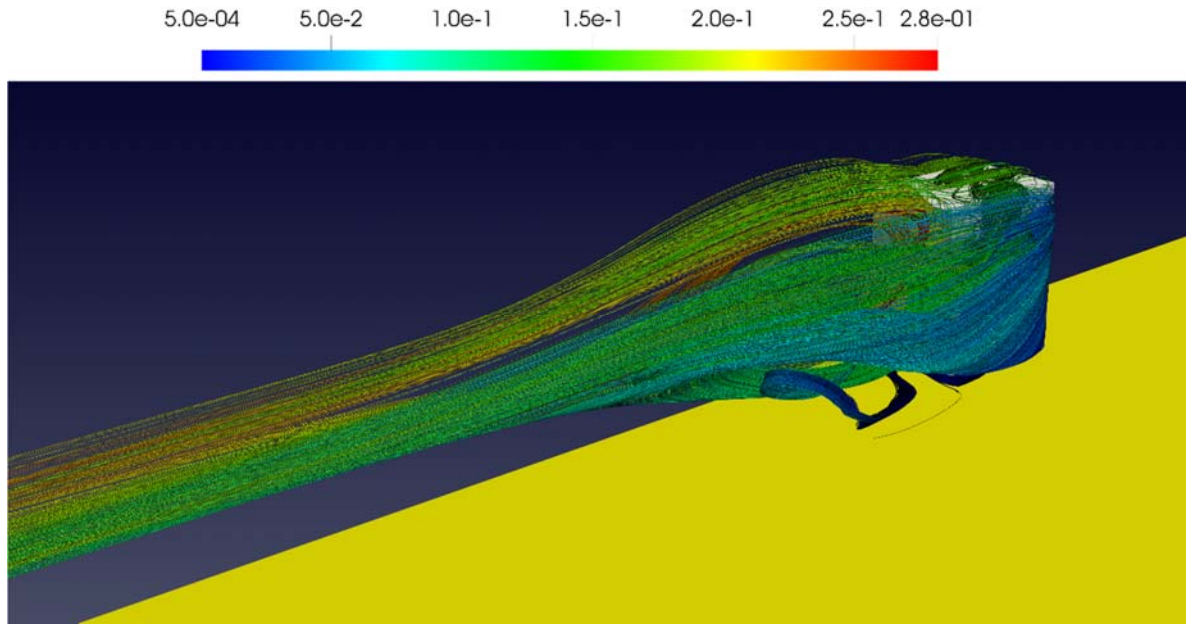
Figure 14 Lagrangian representation of particles distribution and core-radii values

4. CEDVAL B1 array of buildings

Table 8 shows the validation metrics for the velocity components when using the

modified k-ε model with the aerodynamic rough wall functions for the array of

buildings case. The table indicates that this model succeed in the Hit rate, FAC2, and

MG validation tests with a very good results. Figure 15 and Figure 16 represent a

comparison between the numerical and experimental normalized velocity and turbulent

kinetic energy profiles respectively at different locations in the domain. Both profiles

shows conformation between the numerical and the experimental data, and this agrees

with the validation metric results. Figure 17 that represent the blending factor contour

plot show that using this model, the building influence area is detected correctly. From

this simulation, we can conclude that the modified turbulence model can be confidently

used to model wind flow for the cases where we have more than one building in the

domain.

Table 8 Summary of velocity validation metrics when using k- ε model for array of buildings case

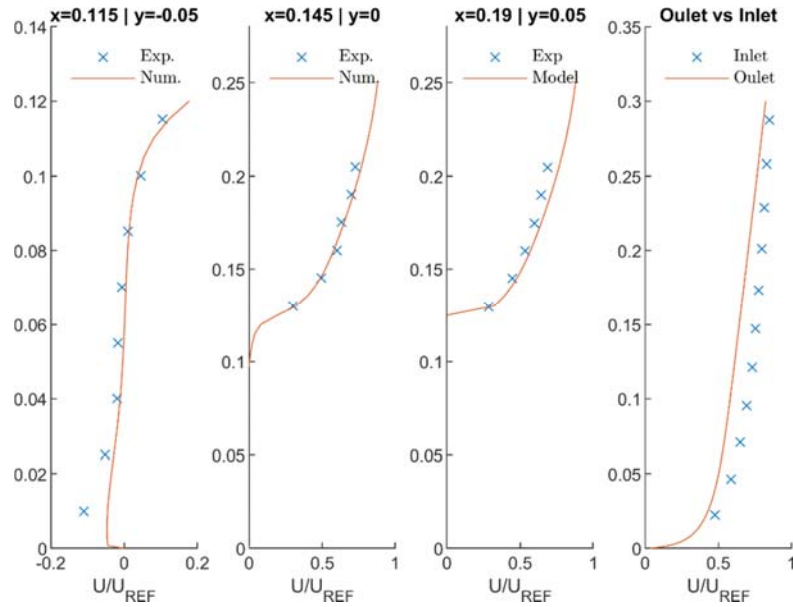| Parameter	u/u_{ref}	v/u_{ref}	w/u_{ref}
Hit rate (≥ 0.66)	0.8169	0.6779	0.7199
FAC2 (≥ 0.5)	0.9338	0.9915	0.7500
MG ($0.7 - 1.3$)	1.0882	1.0000	1.1894

Figure 15 Comparison of experimental data and CFD simulation results for u-velocity components at different positions
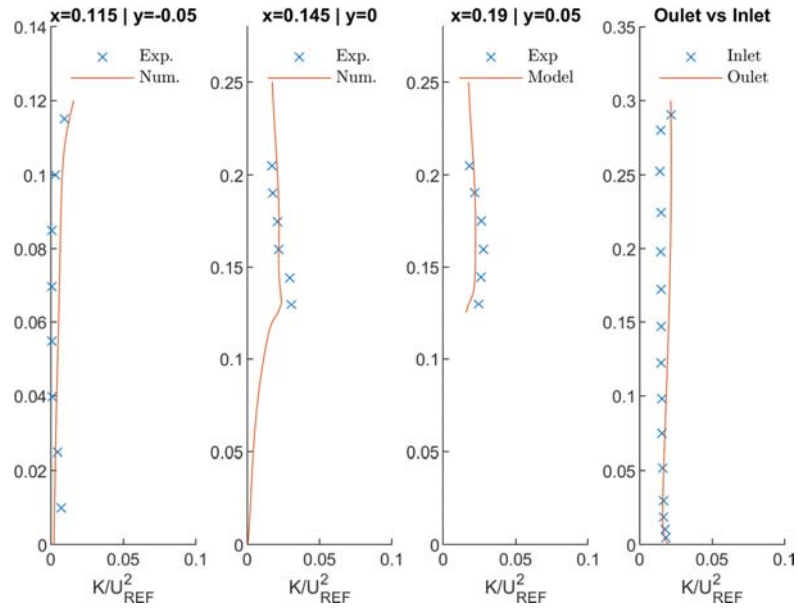
49

Figure 16 Comparison of experimental data and CFD simulation results for turbulent kinetic energy at different positions
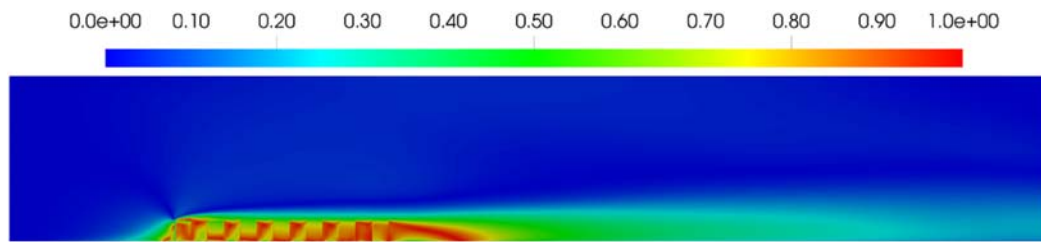
Figure 17 Blending factor for the array of buildings case when using k-ε model

D. Conclusion

In this study, we created a tool for simulating wind flow and pollutant concentration in urban areas. We implemented the diagnostic model that can be used to get approximate but quick results and the prognostic model that is based on the CFD approach with several turbulence closure schemes. To obtain consistency between turbulence model, wall function, and inlet conditions, we used a modification on the *k-ε* model that enables maintaining the inflow conditions through an empty domain for any inlet turbulent kinetic energy profile by adding source terms to the turbulent kinetic

energy and dissipation rate equations. Also, we derived the modifications needed for the k-ω model for the same purpose. Besides, we used a novel approach for wall function based on aerodynamic roughness to overcome the limitations of the sand-grain rough wall functions and to have more flexibility in terms of near wall cell sizes and mesh generation. We simulated the flow in empty domain using the standard and the modified wall functions for different turbulent kinetic energy inlet profiles, and we found that the new wall function formulation can maintain inlet conditions when using the k-ε or k-ω model. Then, numerical simulations for wind field and particles dispersion are performed for the case of single building using the k-ε, k-ω and k-ω SST model, and for wind field for the case of array of buildings using the k-ε model. The simulation results are rigorously tested by statistical validation metrics using extensive data. Accordingly, we found that k-ε and k-ω models can be used to model flow fields, but failed in modeling pollutant dispersion for the case were the source of pollutant is in the leeward side of the building. Whereas, the k-ω SST model that outperforms the k-ε and k-ω models succeed in modeling particles dispersion and wind flow. By comparing the Lagrangian and Eulerian models for simulating gas distribution we can conclude that the use of the particle method with core-radius spreading for diffusion is a good choice as long as the velocity field in the volume that a particle represents is not of a high gradient. A new method can be developed to overcome this limitation based on separating a particle to a group of particles when the value of gradient inside particle volume is high.

REFERENCES

1. Olesen, H.R., et al., *Validation of OML, AERMOD/PRIME and MISKAM using the Thompson wind-tunnel dataset for simple stack-building configurations.* Boundary-layer meteorology, 2009. **131**(1): p. 73-83.
2. Mavroidis, I., R. Griffiths, and D. Hall, *Field and wind tunnel investigations of plume dispersion around single surface obstacles.* Atmospheric Environment, 2003. **37**(21): p. 2903-2918.
3. Sasaki, Y., *An ObJective Analysis Based on the Variational Method.* Journal of the Meteorological Society of Japan. Ser. II, 1958. **36**(3): p. 77-88.
4. Sasaki, Y., *Some basic formalisms in numerical variational analysis.* 1970a.
5. Sasaki, Y., *NUMERICAL VARIATIONAL ANALYSIS FORMULATED UNDER THE CONSTRAINTS AS DETERMINED BY LONGWAVE EQUATIONS AND A LOW-PASS FILTER.* Monthly Weather Review, 1970b. **98**(12): p. 884-898.
6. Sherman, C.A., *A Mass-Consistent Model for Wind Fields over Complex Terrain.* Journal of Applied Meteorology, 1978. **17**(3): p. 312-319.
7. Lange, R., *ADPIC—A Three-Dimensional Particle-in-Cell Model for the Dispersal of Atmospheric Pollutants and its Comparison to Regional Tracer Studies.* Journal of Applied Meteorology, 1978. **17**(3): p. 320-329.
8. Lange, R., *Mathew-ADPIC Model Evalutation of the 1980 ASCOT Geysers Drainage Flow Experiment.* 1984: Lawrence Livermore Lab.
9. Lange, R., *Transferability of a Three-Dimensional Air Quality Model between Two Different Sites in Complex Terrain.* Journal of Applied Meteorology (1988-2005), 1989. **28**(7): p. 665-679.
10. Desiato, F., *A Dispersion Model Evaluation Study for Real-Time Application in Complex Terrain.* Journal of Applied Meteorology (1988-2005), 1991. **30**(8): p. 1207-1219.
11. Ross, D.G., et al., *Diagnostic Wind Field Modeling for Complex Terrain: Model Development and Testing.* Journal of Applied Meteorology (1988-2005), 1988. **27**(7): p. 785-796.
12. Ross, D.G. and D.G. Fox, *Evaluation of an Air Pollution Analysis System for Complex Terrain.* Journal of Applied Meteorology (1988-2005), 1991. **30**(7): p. 909-923.
13. Traci, R., et al., *Development of a wind energy site selection methodology.* Technical Rep., US Department of Energy Report, RLO/2440-11, 1977.
14. Walmsley, J.L., J. Salmon, and P. Taylor, *On the application of a model of boundary-layer flow over low hills to real terrain.* Boundary-Layer Meteorology, 1982. **23**(1): p. 17-46.
15. Walmsley, J.L., et al., *Surface-layer flow in complex terrain: comparison of models and full-scale observations.* Boundary-Layer Meteorology, 1990. **52**(3): p. 259-281.
16. Endlich, R., et al., *A diagnostic model for estimating winds at potential sites for wind turbines.* Journal of Applied Meteorology, 1982. **21**(10): p. 1441-1454.
17. Guo, X. and J. Palutikof, *A study of two mass-consistent models: problems and possible solutions.* Boundary-layer meteorology, 1990. **53**(4): p. 303-332.
18. Ishikawa, H., *Mass-consistent wind model as a meteorological preprocessor for tracer transport models.* Journal of Applied Meteorology, 1994. **33**(6): p. 733-743.

19.   Mathur, R. and L.K. Peters, *Adjustment of wind fields for application in air pollution modeling.* Atmospheric Environment. Part A. General Topics, 1990. **24**(5): p. 1095-1106.

20.   Finardi, S., et al., *A 2–D meteorological pre–processor for real–time 3–D ATD models.* International Journal of Environment and Pollution, 1997. **8**(3-6): p. 478-488.

21.   Tominaga, Y., S. Murakami, and A. Mochida, *CFD prediction of gaseous diffusion around a cubic model using a dynamic mixed SGS model based on composite grid technique.* Journal of Wind Engineering and Industrial Aerodynamics, 1997. **67**: p. 827-841.

22.   Li, X.-X., C.-H. Liu, and D.Y. Leung, *Large-eddy simulation of flow and pollutant dispersion in high-aspect-ratio urban street canyons with wall model.* Boundary-Layer Meteorology, 2008. **129**(2): p. 249-268.

23.   Nazridoust, K. and G. Ahmadi, *Airflow and pollutant transport in street canyons.* Journal of wind engineering and industrial aerodynamics, 2006. **94**(6): p. 491-522.

24.   Delaunay, D., et al., *Numerical and wind tunnel simulation of gas dispersion around a rectangular building.* Journal of wind engineering and industrial aerodynamics, 1997. **67**: p. 721-732.

25.   Jones, W. and B.E. Launder, *The prediction of laminarization with a two-equation model of turbulence.* International journal of heat and mass transfer, 1972. **15**(2): p. 301-314.

26.   Shih, T.-H., et al., *A new k-epsilon eddy viscosity model for high Reynolds number turbulent flows: Model development and validation.* 1994.

27.   Yakhot, V. and S.A. Orszag, *Renormalization group analysis of turbulence. I. Basic theory.* Journal of scientific computing, 1986. **1**(1): p. 3-51.

28.   Kolmogorov, A.N. *Equations of turbulent motion in an incompressible fluid.* in *Dokl. Akad. Nauk SSSR.* 1941.

29.   Wilcox, D.C., *Reassessment of the scale-determining equation for advanced turbulence models.* AIAA journal, 1988. **26**(11): p. 1299-1310.

30.   Wilcox, D.C., *Turbulence modeling for CFD.* Vol. 2. 1998: DCW industries La Canada, CA.

31.   Menter, F.R., *Eddy viscosity transport equations and their relation to the k-ε model.* 1997.

32.   Hirsch, C., *Numerical computation of internal and external flows: The fundamentals of computational fluid dynamics.* 2007: Elsevier.

33.   Franke, J., *The European Cost Action 732–quality assurance and improvement of micro-scale meteorological models.* Wind Engineering, 2009.

34.   Ricci, A., et al., *Impact of turbulence models and roughness height in 3D steady RANS simulations of wind flow in an urban environment.* Building and Environment, 2020. **171**: p. 106617.

35.   Richards, P. and R. Hoxey, *Appropriate boundary conditions for computational wind engineering models using the k-ε turbulence model*, in *Computational Wind Engineering 1*. 1993, Elsevier. p. 145-153.

36.   Cebeci, T. and P. Bradshaw, *Momentum transfer in boundary layers.* hemi, 1977.

37. Launder, B.E. and D.B. Spalding, *The numerical computation of turbulent flows.* Computer Methods in Applied Mechanics and Engineering, 1974. **3**(2): p. 269-289.

38. Blocken, B., T. Stathopoulos, and J. Carmeliet, *CFD simulation of the atmospheric boundary layer: wall function problems.* Atmospheric Environment, 2007. **41**(2): p. 238-252.

39. Yang, Y., et al., *New inflow boundary conditions for modelling the neutral equilibrium atmospheric boundary layer in computational wind engineering.* Journal of Wind Engineering and Industrial Aerodynamics, 2009. **97**(2): p. 88-95.

40. Parente, A., et al., *Improved k–ε model and wall function formulation for the RANS simulation of ABL flows.* Journal of wind engineering and industrial aerodynamics, 2011a. **99**(4): p. 267-278.

41. Pendergast, M.M., *Estimating diffusion coefficients from meteorological data.* 1976, ; Du Pont de Nemours (E.I.) and Co., Aiken, SC (USA). Savannah River Lab. p. Medium: ED; Size: Pages: 45.

42. Parente, A., et al., *A comprehensive modelling approach for the neutral atmospheric boundary layer: consistent inflow conditions, wall function and turbulence model.* Boundary-layer meteorology, 2011b. **140**(3): p. 411.

43. Brost, R. and J. Wyngaard, *A model study of the stably stratified planetary boundary layer.* Journal of the Atmospheric Sciences, 1978. **35**(8): p. 1427-1440.

44. Bechmann, A., *Large-eddy simulation of atmospheric flow over complex terrain.* 2006, Risø National Laboratory.

45. Hargreaves, D. and N.G. Wright, *On the use of the k–ε model in commercial CFD software to model the neutral atmospheric boundary layer.* Journal of wind engineering and industrial aerodynamics, 2007. **95**(5): p. 355-369.

46. Longo, R., et al., *Advanced turbulence models and boundary conditions for flows around different configurations of ground-mounted buildings.* Journal of Wind Engineering and Industrial Aerodynamics, 2017. **167**: p. 160-182.

47. Fick, A., *On liquid diffusion.* Annalen der Physik und Chemie, 1855.

48. Hugo B. Fischer, E.J.L., Robert C. Y. Koh, Jorg Imberger, Norman H. Brooks, *Mixing in Inland and Coastal Waters.* 1979, New York: Academic Press.

49. Tominaga, Y. and T. Stathopoulos, *Turbulent Schmidt numbers for CFD analysis with various types of flowfield.* Atmospheric Environment, 2007. **41**(37): p. 8091-8099.

50. Leitl, P.D.B. *CEDVAL at Hamburg University Compilation of Experimental Data for Validation of Microscale Dispersion Models.* 1998; Available from: https://mi-pub.cen.uni-hamburg.de/index.php?id=432.

51. Hoxey, R.P., P.J. Richards, and J.L. Short, *A 6 m cube in an atmospheric boundary layer flow: Part 1. Full-scale and wind-tunnel results.* Wind and Structures, An International Journal, 2002. **5**(2-4): p. 165-176.

52. Schatzmann, M., H. Olesen, and J. Franke, *COST 732 MODEL EVALUATION CASE STUDIES: APPROACH AND RESULTS.* 2010.

53. Yu, H. and J. Thé, *Simulation of gaseous pollutant dispersion around an isolated building using the k–ω SST (shear stress transport) turbulence model.* Journal of the Air & Waste Management Association, 2017. **67**(5): p. 517-536.

54. Kakosimos, K. and M. Assael, *Application of Detached Eddy Simulation to neighbourhood scale gases atmospheric dispersion modelling.* Journal of hazardous materials, 2013. **261**: p. 653-668.
55. Guideline, V., *Environmental Meteorology–Prognostic Micro-scale Wind Field Models–Evaluation for Flow Around Buildings and Obstacles.* 2005.
56. Gorlé, C., J. van Beeck, and P. Rambaud, *Dispersion in the wake of a rectangular building: validation of two Reynolds-averaged Navier–Stokes modelling approaches.* Boundary-layer meteorology, 2010. **137**(1): p. 115-133.
57. Hanna, S.R., O.R. Hansen, and S. Dharmavaram, *FLACS CFD air quality model performance evaluation with Kit Fox, MUST, Prairie Grass, and EMU observations.* Atmospheric Environment, 2004. **38**(28): p. 4675-4687.